

A flexible, fast and benchmarked vectorial model for focused laser beams

QINGFENG LI^{1,*}, MAXIME CHAMBONNEAU¹, MARKUS BLOTHE¹, HERBERT GROSS^{1,2}, AND STEFAN NOLTE^{1,2}

¹Institute of Applied Physics, Abbe Center of Photonics, Friedrich-Schiller-University Jena, Albert-Einstein-Str. 15, 07745 Jena, Germany

²Fraunhofer Institute for Applied Optics and Precision Engineering, Albert-Einstein-Str. 7, 07745 Jena, Germany

*Corresponding author: qingfeng.li@uni-jena.de

Compiled January 8, 2021

In-bulk processing of materials by laser has largely evolved over the last decades and still reveals new scientific and industrial potential. The development of any in-bulk processing application relies on the knowledge of laser propagation especially volumetric field distribution near the focus. Many commercial programs can simulate this, but, in order to adapt them, or to develop new methods, researchers need to create their own software. Besides, people also need to know the actual field distribution near the focus to evaluate their assumptions in the simulation. To help people easily get their access to this knowledge, we decided to release our high-precision field distribution measuring method as well as our in-house software InFocus [1], under the Creative Commons 4.0 License, an open-source license. Our measurements provide 300-nm longitudinal resolution and diffraction limited lateral resolution. And the in-house software allows fast vectorial analysis of the focused volumetric field distribution in the bulk. It considered the lens induced spherical aberrations as well as the planar interface induced spherical aberrations. The simulations and measurements are systematically compared. © 2021 Optical Society of America

<http://dx.doi.org/10.1364/ao.XX.XXXXXX>

1. INTRODUCTION

In the last two decades, laser processing in the bulk of optical materials has attracted intensive attention in a wide range of academic researches and industrial engineering. In-bulk laser direct writing enables precise three-dimensional structuring and has allowed many innovative applications include the fabrication of channels [2–5], waveguides [6–10], gratings [11], binary data storage [12], and photonics quantum gates [13, 14]. The nature of the in-bulk processing also innovates new manufacturing procedures such as bonding [15–19] and dicing [20] of the brittle materials. Among all the potential applications, the precise description and control of the laser focusing and the energy deposition are crucial. Numbers of experimental and theoretical investigations on the laser propagation and the energy absorption have been intensively carried [21–25].

The focus of the electromagnetic (EM) field can be rigorously described by the finite difference time domain (FDTD) method [26], however in general it requires significant computational time. Considerable effort has been devoted to designing propagation equations that on one hand preserve their computational simplicity and on the other hand preserve the correct description of nonparaxial and vectorial effects. In the nonlinear propagation regime, only until recently, the unidirectional Hertz vector propagation equation (UHPE) [27, 28] was derived to provide

a seamless transition from Maxwell's equations to the various envelope-based model, that considerably reduces the computational effort. Simulations of the UHPE, require starting from input conditions, i.e., from the Hertz vector in a plane $z = z_0$. When the focusing elements have a high numerical aperture (NA), the input conditions are then determined by a phase correction to the field that simulates the action of the focusing element. The input conditions for the UHPE were constructed by a detailed calculation of diffraction by vectorial diffraction integrals (VDIs) [29, 30], i.e. the linear propagation model. However, even though the vectorial effects have been considered by VDIs, the residual aberrations of the focusing elements are often ignored, which leads to deviation from the correctness in the real laser processing conditions.

The purpose of this work is to have accurate descriptions of these input conditions by taking all the potential aberrations that may involve with the laser in-bulk focusing, and to have fast analyses with a proper transformation of the VDIs.

One of the most widely used integral for analyzing the vectorial diffraction is the Debye-Wolf integral. As demonstrated by Leutenegger *et al.* [31], the 3D vectorial field distribution at the focus can be computed plane by plane under a proper transformation of the original Debye-Wolf integral. At a given axial position, the EM field in this plane is obtained by a two-dimensional

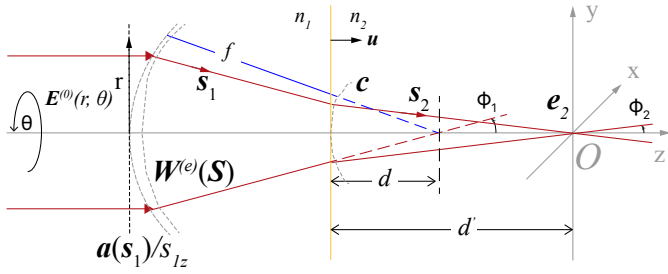


Fig. 1. Diagram showing laser focused by a lens into two media separated by a planar interface.

Fourier transform. Lin *et al.* [32] have also demonstrated that this method is applicable to focusing through an interface between two mediums of mismatched refractive index. In this paper, we further adapt this method to the real lens conditions and provide a fast analysis tool which can evaluate the actual EM field distribution at the focus of the lens whose residual aberrations cannot be neglected. Meanwhile, a non-destructive method is introduced to provide 300-nm longitudinal and diffraction limited lateral resolution measurements of the in-bulk volumetric intensity distribution. The experimental result benchmarked our numerical methods.

2. MODEL DESCRIPTIONS

A. 3D-FT representation of the field vectors near the focus

Using the form developed by Richards and Wolf [33], the time-dependent field in the image regime of a system can be expressed by equation Eq. (1). \mathbf{e} and \mathbf{h} are the time-independent electric and magnetic vectors.

$$\begin{aligned} \mathbf{E}(x, y, z, t) &= \Re\{\mathbf{e}(x, y, z)e^{-i\omega t}\}, \\ \mathbf{H}(x, y, z, t) &= \Re\{\mathbf{h}(x, y, z)e^{-i\omega t}\}. \end{aligned} \quad (1)$$

At any point $\mathbf{P}(x, y, z)$ in the image space, the electric and magnetic vector express in the form as a summation of the plane waves that are leaving the aperture:

$$\begin{aligned} \mathbf{e}(x, y, z) &= -\frac{ik}{2\pi} \iint_{\Omega} \frac{\mathbf{a}(s_x, s_y)}{s_z} e^{ik[\Phi(s_x, s_y) + s_x x + s_y y + s_z z]} ds_x ds_y, \\ \mathbf{h}(x, y, z) &= -\frac{ik}{2\pi} \iint_{\Omega} \frac{\mathbf{b}(s_x, s_y)}{s_z} e^{ik[\Phi(s_x, s_y) + s_x x + s_y y + s_z z]} ds_x ds_y \end{aligned} \quad (2)$$

where $\Phi(s_x, s_y)$ is the aberration function which describes the optical path difference between the aberrated and the spherical wavefront along \mathbf{s} , \mathbf{a} and \mathbf{b} are the electric and magnetic strength vectors of the unperturbed electric and magnetic fields in the exit aperture, k is the wave number, and Ω is the solid angle formed by all the geometrical optics ray. The phase factor shown in equation Eq. (2) contains two parts, one is the scalar product of vector \mathbf{s} and vector \mathbf{r}_p , another is the vectorial aberration function. In this section henceforth we only discuss about the electric field since, apart from the strength vector, the two equations in Eq. (2) are the same.

Now lets consider a laser in-bulk focusing senario. As shown in Fig. 1, after the focusing lens it consist of materials 1 and 2 with refractive indices n_1 and n_2 .

In material 1 and at the interface ($z = -d$), the electric field is

given by

$$\begin{aligned} \mathbf{e}_1(x, y, -d) &= -\frac{ik_1}{2\pi} \iint_{\Omega} \mathbf{C}(\vec{s}) \\ &\times \exp[ik_1(s_{1x}x + s_{1y}y - s_{1z}d)] ds_{1x} ds_{1y} \end{aligned} \quad (3)$$

where

$$\mathbf{C}(\vec{s}) = \frac{\mathbf{a}(s_{1x}, s_{1y})e^{ik_1\Phi(s_{1x}, s_{1y})}}{s_{1z}} \quad (4)$$

by letting the strength vector $\mathbf{a}(s_{1x}, s_{1y})$ absorb the aberration phase factor $e^{ik_1\Phi(\vec{s})}$, the phase factor in Eq. (3) contains only the scalar product of vector \mathbf{s} and vector \mathbf{r}_p . And the new strength vector $\mathbf{C}(\vec{s})$ is turned to be a complex strength vector.

Since there is no optical coating for all the cubical materials presented in this paper, we assumed that each plane wave components refracting at the interface obeys the Fresnel's law. To determind the transmitted field in the second material, we also assumed that the field in the second material is constructed by the superposion of refracted plane waves. As the complex strength vector of the plane wave upon the interface is described as $\mathbf{C}(\vec{s})$, the strength vector of the transmitted plane wave can be described as a linear function of $\mathbf{C}(\vec{s})$, i.e, $\mathbf{T} \cdot \mathbf{C}(\vec{s})$, where \mathbf{T} is a refraction operator which is a function of angle of incident and n_1, n_2 . Therefore, the transmitted field in the second material can be written as

$$\begin{aligned} \mathbf{e}_2(x, y, -d) &= -\frac{ik_1}{2\pi} \iint_{\Omega_1} \mathbf{T} \cdot \mathbf{C}(\vec{s}) \\ &\times \exp[ik_1(s_{1x}x + s_{1y}y - s_{1z}d)] ds_{1x} ds_{1y} \end{aligned} \quad (5)$$

On the other hand, as Török *et al.* [34] suggested, we can also represent the field in the second material again as superposion of plane waves, which is a solution of time-dependent wave equation and can be written as

$$\mathbf{e}_2(\mathbf{r}_p) = -\frac{ik_2}{2\pi} \iint_{\Omega_2} \mathbf{F}(\vec{s}_2) \exp(ik_2\vec{s}_2 \cdot \mathbf{r}_p) ds_{2x} ds_{2y}. \quad (6)$$

One can notice that Eq. (5) is the boundary condition of Eq. (6). Now let's establish the relation between \vec{s}_1 and \vec{s}_2 .

According to the law of refraction,

$$k_1(\vec{u} \times \vec{s}_1) = k_2(\vec{u} \times \vec{s}_2), \quad (7)$$

where \vec{u} is the unit vector that normal to the interface. When a planar interface is presented $\vec{u} = (0, 0, 1)$, and we have

$$k_1 s_{1x} = k_2 s_{2x}, \quad k_1 s_{1y} = k_2 s_{2y}. \quad (8)$$

By taking the coordinate transformation, equation Eq. (6) yields

$$\begin{aligned} \mathbf{e}_2(\mathbf{r}_p) &= -\frac{ik_2}{2\pi} \iint_{\Omega_1} \mathbf{F}(\vec{s}_2) \\ &\times \exp(ik_2\vec{s}_2 \cdot \vec{r}_p) J_0(s_{1x}, s_{1y}; s_{2x}, s_{2y}) ds_{1x} ds_{1y}, \end{aligned} \quad (9)$$

where J_0 is the Jacobian of the coordinate transformation obtained from equation Eq. (8):

$$J_0 = \left(\frac{k_1}{k_2}\right)^2, \quad (10)$$

As equation Eq. (9) must satisfies the boundary condition represented by equation Eq. (5), we have

$$\mathbf{F}(\vec{s}_1, \vec{s}_2) = \left(\frac{k_2}{k_1}\right) \mathbf{T} \cdot \mathbf{C}(\vec{s}) \exp[id(k_2 s_{2z} - k_1 s_{1z})]. \quad (11)$$

By substituting into equation Eq. (9) we obtain the electric field in the second material:

$$\begin{aligned} \mathbf{e}_2(x, y, z) = & -\frac{ik_2^2}{2\pi k_1} \iint_{\Omega_1} \mathbf{T} \cdot \mathbf{C}(\mathbf{s}) \\ & \times \exp[id(k_2 s_{2z} - k_1 s_{1z})] \exp(ik_2 s_{2z} z) \\ & \times \exp[ik_1(s_{1x}x + s_{1y}y)] ds_{1x} ds_{1y}. \end{aligned} \quad (12)$$

The first phase factor $\exp[id(k_2 s_{2z} - k_1 s_{1z})]$ stands for the aberration induced by the interface. The second phase factor $\exp(ik_2 s_{2z} z)$ accounts for the phase accumulation when propagating along the z-axis, whereas the third term $\exp[ik_1(s_{1x}x + s_{1y}y)]$ represents the phase difference of the wave front at off-axis points (x,y,z) with respect to the on-axis point (0,0,z).

Depends on the coordinate one has choosen, the following forms of the wave vectors are equivalent:

$$\vec{k}_1 = \begin{pmatrix} k_{1x} \\ k_{1y} \\ k_{1z} \end{pmatrix} = k_1 \begin{pmatrix} -s_{1x} \\ -s_{1y} \\ s_{1z} \end{pmatrix} = k_1 \begin{pmatrix} -\sin \phi_1 \cos \theta \\ -\sin \phi_1 \sin \theta \\ \cos \phi_1 \end{pmatrix}, \quad (13)$$

$$\vec{k}_2 = \begin{pmatrix} k_{2x} \\ k_{2y} \\ k_{2z} \end{pmatrix} = k_2 \begin{pmatrix} -s_{2x} \\ -s_{2y} \\ s_{2z} \end{pmatrix} = k_2 \begin{pmatrix} -\sin \phi_2 \sin \theta \\ -\sin \phi_2 \cos \theta \\ \cos \phi_2 \end{pmatrix}.$$

Therefore, $ds_{1x} ds_{1y}$ can be written as $dk_{1x} dk_{1y}/k_1^2$ and the interface induced aberration can be written as

$$\Psi(\phi_1, \phi_2, d) = d(n_2 \cos \phi_2 - n_1 \cos \phi_1). \quad (14)$$

The spherical-polar form of the complex strength vector after the interface is

$$\mathbf{C}(\phi_1, \phi_2, r, \theta) = \mathbf{T}(\phi_1, \phi_2, \theta) \cdot \mathbf{a}(r, \theta) e^{ik_1 \Phi(r, \theta)} / \cos \phi_1. \quad (15)$$

By using $\mathbf{c}(\phi_1, \phi_2, r, \theta)$ to brief note $\mathbf{T}(\phi_1, \phi_2, \theta) \cdot \mathbf{a}(r, \theta) e^{ik_1 \Phi(r, \theta)}$, Eq. (12) can be finally rewritten as

$$\begin{aligned} \mathbf{e}_2(x, y, z, d) = & -\frac{ik_2^2}{2\pi k_1^3} \iint_{r < R} [\mathbf{c}(\phi_1, \phi_2, \theta) e^{ik_0 \Psi(\phi_1, \phi_2, d)} e^{ik_2 z} / \cos \phi_1] \\ & \times \exp[-i(k_{1x}x + k_{1y}y)] dk_{1x} dk_{1y}. \end{aligned} \quad (16)$$

By using Leutenegger's method [31], setting $|\mathbf{c}| = 0$ when $r > R$, the Debye-Wolf intergral is now expressed as the Fourier transform of the field distribution after the interface formed by the two material. And finally result in

$$\mathbf{e}_2(x, y, z, d) = -\frac{ik_2^2}{2\pi k_1^3} \mathcal{F}[\mathbf{c}(\phi_1, \phi_2, \theta) e^{ik_0 \Psi(\phi_1, \phi_2, d)} e^{ik_2 z} / \cos \phi_1]. \quad (17)$$

As inspired by Leutenegger [31], we used the chirped Z-transform (CZT) algorithm [35] for the Fourier transformation. With this algorithm, it (a) allows breaking the relationship between the sampling points (M) over the aperture radius and the minimal sampling points (N) for fast Fourier transform (FFT), (b) allows an implicit frequency offset, and (c) internalizes the zero padding. Applying this generalization, one can adapt the sampling step in the focus field independently of the sampling step in the input field, introduce an additional shift of the region of interest, and finally improve the computational efficiency.

B. Representation of the complex strength vector

To determind the complex strength vector \mathbf{c} , let's assume that a linear polarized wave incident upon a lens. By choosing the corresponding Cartesian coordinate and letting the y and z-component of the incident electric field as zero, the incident electric strength vector can be written as

$$\mathbf{E}^{(0)} = \begin{pmatrix} E_0 \\ 0 \\ 0 \end{pmatrix}. \quad (18)$$

According to Török *et al.* [34], the transform relation between the incident vector and the refracted vector after the interface can be expressed by a refraction operator \mathbf{T} . This operator has a matrix form of

$$\mathbf{T} = A(\phi_1) \begin{bmatrix} a_{11} & a_{12} & a_{13} \\ a_{12} & a_{22} & a_{23} \\ -a_{13} & a_{23} & a_{33} \end{bmatrix}. \quad (19)$$

with

$$\begin{aligned} a_{11} &= \tau_p \cos^2 \theta \cos \phi_2 + \tau_s \sin^2 \theta, \\ a_{12} &= (\tau_p \cos \phi_2 - \tau_s) \cos \theta \sin \theta, \\ a_{13} &= \tau_p \cos \theta \sin \phi_2, \\ a_{22} &= \tau_s \cos^2 \theta + \tau_p \cos \phi_2 \sin^2 \theta, \\ a_{23} &= \tau_p \sin \theta \sin \phi_2, \\ a_{33} &= \tau_p \cos \phi_2, \end{aligned}$$

where τ_s and τ_p are the Fresnel transmission coefficients for s-polarized and p-polarized light, respectively. The function $A(\phi_1)$ is an apodization function that depends on the lens. And when the system obeys Abbe's sine condition, i.e, is aplanatic, then

$$A(\phi_1) = f l_0 \sqrt{\cos \phi_1} \quad (20)$$

where f_0 is the focal length of the lens in vacuum and l_0 is an amplitude factor. It is assumed that the Abbe's sine condition is valid in this step, as it is usually fullfilled in a corrected microscopic lens or in a single spherical lens with the stop located at the lens.

To represent the aberration phase factor and to scale it in the scale of wavelength λ , the aberration factor $e^{ik_1 \Phi(r, \theta)}$ is rewritten as $e^{i2\pi W(r, \theta)}$. To describe a circular lens induced wavefront aberration and calculate the deviation of the wavefront to an ideal spherical shape, one widely used method is to represent it by Zernike polynomials.

By using the vendors provided lens data, the aberration function can be calculated in the form of superposion of Zernike polynomials through any home made ray tracing program or commercial softwares such as Zemax or Code V. In this paper, we used Zemax to calculate the aberration function and used the notation convention defined by R. Noll [36] (so called Zernike standard polynomials):

$$W = \sum_{i=1}^{37} c_i Z_i(\rho, \theta_0), \quad (21)$$

where c_i is the orthonormal Zernike coefficient computed by Zemax, Z_i is the corresponding Zernike standard polynomial and dimensionless radius $\rho = r/r_{max}$ that normalized to the radius of the entrance pupil.

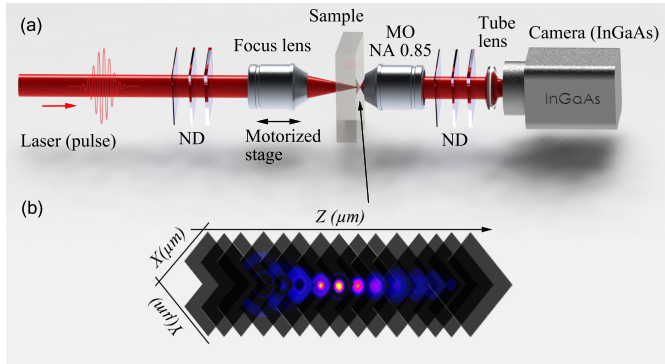


Fig. 2. Illustration of in-bulk propagation imaging processes. (a) Experimental setup, MO: microscope objective lens, ND: neutral density filters. (b) Intensity distribution near the focal region reconstructed from the stacking of captured images applying a z-scan.

Finally from equations Eq. (15) and Eq. (18)-Eq. (21), the complex strength vector after the interface can be written as:

$$\mathbf{c} = f l_0 \sqrt{\cos \phi_1} \times \begin{bmatrix} a_{11} & a_{12} & a_{13} \\ a_{12} & a_{22} & a_{23} \\ -a_{13} & a_{23} & a_{33} \end{bmatrix} \begin{bmatrix} e^{i2\pi W} & 0 & 0 \\ 0 & e^{i2\pi W} & 0 \\ 0 & 0 & e^{i2\pi W} \end{bmatrix} \begin{bmatrix} E_0 \\ 0 \\ 0 \end{bmatrix}. \quad (22)$$

By substituting Eq. (22) into Eq. (12), a CZT algorithm based highly-efficient propagation model is complete, it allows fast in-focus fields calculation by taking both lens-induced and interface-induced aberration into account.

3. EXPERIMENTAL ARRANGEMENT

A. Propagation imaging

Propagation imaging methods have been widely used to investigate the linear or nonlinear optical effects in a medium [37, 38]. In this paper, to have a systematic comparison with the numerical results, we introduced the non-destructive measurements on the in-bulk volumetric intensity distributions which rely on (i) the focusing of the laser beam at the exit surface of the sample with desired thickness, and (ii) an inverted microscope working in transmission for imaging the beam profile in the xy plane for various positions of the focusing objective along the propagation direction z. The experimental set-up is schematically depicted in Fig. 2.

The measurements can explicitly divide into two steps. The first step consist in focusing the laser beam with identical characteristics (beam size, spectrum, phase distribution, etc.) as the simulation. For the ultrashort pulse laser, before focusing, the pulse energy is kept as low as possible (typically, on the order of 18 pJ) for avoiding nonlinear propagation. In this case, we can set the maximum fluence position as the reference and overlap it with the exit surface of the cubical sample. The second step consists in imaging the exit surface of the sample with the inverted microscope working in transmission along the z-axis. This microscope is composed of an infinity-corrected objective lens whose NA is larger than the focusing elements, a tube lens and an InGaAs array (Xenics, Bobcat 320). In this paper, the NA of the imaging objective lens is kept as 0.85 and its focal plane is precisely adjusted at the exit surface of the sample under the white

light illumination by a manual translation stage. When there is no sample (focus in air), this plane can be arbitrarily chosen. Thanks to a precision stage (Physik Instrumente, M-126DC1), the laser intensity evolution along the z-axis is recorded by alternating 100-nm movements of the focus lens (corresponding to $n \times 100$ -nm displacement in a sample with refractive index of n), and image acquisitions by the camera. The stack of images is then post-processed for reconstructing the fluence distribution as follows. Firstly, due to the jitter of the laser, some of the recorded images may show a much higher maximum intensity compare to both the preceding and the following one. These rare outlier images are replaced by the average of the preceding and the following images. Then, in the corner of each image, the noise is calculated as the average of the pixel amplitude, and subsequently subtracted to all pixels. The image containing the maximum grey level is found for a normalization of the whole stack. Two images before and after this latter image are defined for evaluating and correcting the residual tilt of the collecting objective lens with respect to the incoming beam. Finally, the beam propagation is reconstructed by displaying a cross section (along x or y) of each image at the center of the beam.

B. Materials

To demonstrate the universality of our methods, propagation imaging experiments have been carried out for four different focusing elements under two laser platforms. The first platform is based on a prototype TRUMPF TruMicro 2030 Femto Edition laser with a wavelength λ of 1030 nm and a pulse duration of 265 fs. The second one is based an erbium-doped fiber laser (Raydiance Inc, Smart Light 50) with a wavelength λ of 1555 nm and a pulse duration of 9.8 ps. The average power stabilities of both lasers are $< 1\%$. Two single lens (Thorlabs, LA1951-C and C240TME-C) and a $50\times$ microscopic objective lens (Mitutoyo, Apo NIR) are tested under the Raydiance laser platform ($1/e^2$ radius of the input Gaussian beam is 5.2-mm). A $20\times$ microscopic objective lens (Mitutoyo, Apo NIR) is tested under the TruMicro 2030 platform, the input beam profiles are shaped through amplitude modulation (slit) or phase modulation (phase plate). To represent the residual aberrations of the two single lens, the nonzero terms of the Zernike standard coefficients of the two single lens are calculated according to our experimental conditions and listed in the Appendix A. The laser beams are focused in the air or the bulk of a crystalline silicon (c-Si) with $\langle 100 \rangle$ orientation and $200\text{-}\Omega \cdot \text{cm}$ resistivity. Therefore, the refractive index of the focused-in medium are 1 and 3.475 ($\lambda = 1555$ nm). Detailed information of the materials used in the experiment are listed in Tab. 1.

4. RESULTS AND DISCUSSIONS

In this section we have systematically compared our numerical results with the experiments. Under the in-air focus condition, the experimental results benchmarked our numerical model. The further numerical investigations of in-silicon focus condition, on the other hand, pointed out a limitation of the experimental method.

A. Gaussian beam focused by aspheric lens in air

To achieve in-bulk processing, tightly focused laser beams are often required. A cost-efficient solution to get the diffraction-limited high quality tight focusing is to use the aspheric lens. However, it is worth noting that a single aspheric lens is also not aplanatic, the higher order aberrations should be considered. In

Vendor, Lens	f [mm]	NA	Φ [mm]	$1/e^2$ radius [mm]	λ [nm]	Focused-in medium
Thorlabs, LA1951-C	25.3	-	25.4	5.2	1555	Air
Thorlabs, C240TME-C	8.0	0.50	8.0	5.2	1555	Air
Mitutoyo, 20 \times Plan Apo NIR	10.0	0.4	8	User defined	1030	Air
Mitutoyo, 50 \times Plan Apo NIR HR	4.0	0.65	5.2	5.2	1555	Si

Table 1. Prescription data of the lens for the demonstrations. f is the focal length, NA is the numerical aperture, Φ is the entrance aperture diameter, ω is the incident beam waist, λ is the central wavelength of the incident beam and n_2 is the refractive index of the focused-in medium.

this paper, a Thorlabs C240TME-C aspheric lens with NA = 0.5 is used for the demonstration. As the $1/e^2$ radius of the input beam is 5.2-mm, the overfilled factor regards to the entrance pupil ($\Phi = 8\text{ mm}$) is 1.3. Therefore, to calculate the aberrations induced by this lens, in Zemax the apodization factor G (refers to the rate of decrease of the beam amplitude as a function of radial pupil coordinate) is set as $\sqrt{1/1.3}$, i.e. 0.877. The amplitude is normalized to unity at the center of the pupil, and on the other points of the entrance pupil the amplitude is given by $A(\rho) = e^{-G\rho^2}$, where ρ is the normalized pupil coordinate. Under this approximation, the aberration induced by the lens is calculated and represented by the standard Zernike coefficients. In Tab. A1 we list the nonzero coefficients up to the 37th term. As a first demonstration, the focused-in medium is air and the corresponding refractive index is 1. Based on Eq. (17) and Eq. (22), the normalized intensity distribution near the focus is calculated and presented in Fig. 3 (c-d). By applying the method presented in section 4 (A), the corresponding experimental results are presented in Fig. 3 (a-b). As described in Tab. 1, the collimated laser beam with wavelength of 1555-nm is propagated from the left to the right and focused by the aspherical lens C240TME-C under the normal incident condition. Fig. 3 (a) (c) shown the normalized longitudinal intensity distributions and Fig. 3 (b) (d) shown the intensity distribution at the focal plane. The overall distributions are very similar. To quantitatively evaluate how good the simulation results fit with the experimental one, in Fig. 3 (e-f) the normalized experimental intensity profiles are plot against the simulated one. Meanwhile, the absolute value of the intensities differences are also point-by-point plotted along each axis. Based on these quantitative analyses, the root-mean-square deviation (RMSD) of those two normalized intensities are calculated for each axis. As shown in Fig. 3 (e), by setting the intensity maximized position as the origin, the intensity profiles and their differences are plot from $-5\text{ }\mu\text{m}$ to $5\text{ }\mu\text{m}$. The experimental beam width ($1/e^2$) is measured as $2.64\text{ }\mu\text{m}$, and the simulated one is $2.93\text{ }\mu\text{m}$. In this transverse direction, the above mentioned RMSD is calculated as 0.0305. We applied the same methods to the results along the longitudinal direction. As shown in Fig. 3 (f), the normalized intensities profiles are compared along the z-axis. The RMSD of the longitudinal profiles is calculated as 0.0322. To anchor a reference, we also simulated the intensity distribution near the focus without considering the influence of the aberration. In this case, the RMSD of the normalized profiles along x, z-axis are 0.0382 and 0.0365. In other words, by taking the aberration induced by the C240TME-C lens into account, the RMSDs have decreased by 20.2% and 11.8% along the x and z-axis correspondingly.

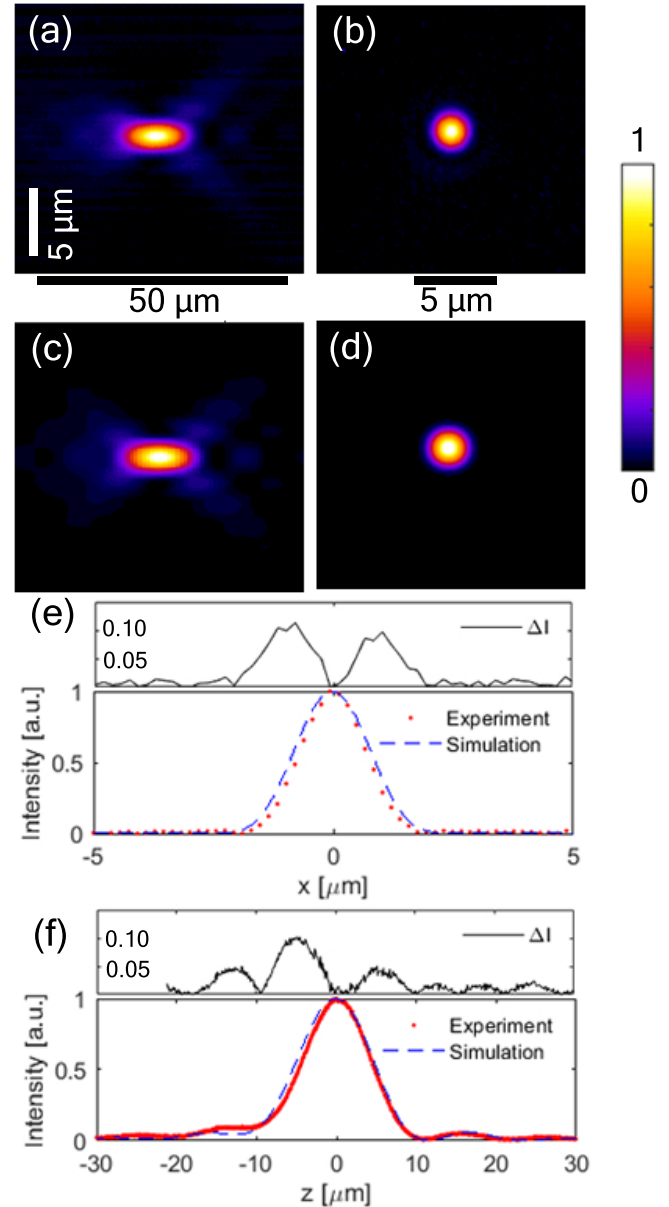


Fig. 3. Intensity distribution near the focus of an aspherical lens (C240TME-C) in air with a Gaussian beam as the input. (a) Experimentally measured intensity along x-z plane; (b) experimentally measured intensity at the focal plane; (c) simulated intensity along x-z plane; (d) simulated intensity at the focal plane. The comparison of the intensity profiles at the focal plane along the x-axis (e); and along the z-axis (f).

B. Gaussian beam focused by plano-convex lens in air

The plano-convex lens is one of the simplest converging lens that has been widely used to focus collimated light. However, even the asymmetry design can minimize the spherical aberration by letting the curved surface face towards the collimated beam, it cannot be completely reduced. In this demonstration, we chose a plano-convex lens (Thorlabs LA1951-C) with $f = 25.3 \text{ mm}$ and used the two methods mentioned in section 2 to evaluate the intensity distribution at its focus. The same collimated laser beam that used in the previous section is focused by this lens in air. To calculate the lens induced aberrations, in Zemax the beam amplitude is normalized to unity at the center of the pupil, at other points in the entrance pupil the amplitude is given by $A(\rho) = e^{-G\rho^2}$, where $G = 4$ and ρ is the normalized pupil coordinate. Under this approximation, the aberration induced by the lens is calculated and represented by the standard Zernike coefficients. In Tab. A1 the nonzero coefficients are listed up to the 37th term. Finally, the normalized intensity distribution near the focus can be calculated based on equations Eq. (17) and Eq. (22) and presented in Fig. 4 (c-d). The corresponding experimental results are presented in Fig. 4 (a-b).

Fig. 4 (a) (c) show the normalized longitudinal intensity distributions and Fig. 4 (b) (d) show the intensity distribution at the focal plane. To quantitatively evaluate the goodness of fit, in Fig. 4 (e-f), we plot the normalized intensity value along the x and y central segment at the focal plane.

As shown in Fig. 4 (e), along the x-axis, the experimental beam width at $1/e^2$ is measured as $10.6 \mu\text{m}$ and the simulated one is $11.4 \mu\text{m}$. The RMSD of the two profiles is 0.051. Similar comparisons are applied to the profiles along the y-axis. The experimental beam width is measured as $11.3 \mu\text{m}$, the simulated one is $11.4 \mu\text{m}$ and the RMSD is 0.046. From the quantitative comparison one can notice that, deviating from the simulated results, the experimental one exhibits the elliptical feature. This deviation is most probably due to the fact that the during the simulation the incident beam has been oversimplified as a circular Gaussian beam. Except of that, the simulated results fit well with the experiment.

It is also worth noting that, given that the experimental results shown in Fig. 4 (a) are composed by 6000 individual frames, at the left-hand side of this figure some frames are misaligned due to the environment disturb such as air flows and vibrations. Despite that, one can notice that the aberration features as well as the overall lengths of the focal regime are identical.

C. Exotic beams focused by objective lens in air

The microscope objective lens are also widely used for laser beam focusing and material processing. With a proper design, the aberrations can be well corrected under a certain wavelength. In this section, we chose the $20\times$ Mitutoyo Plan Apo objective lens (NA = 0.4) as the focus lens. The central wavelength of the laser source is 1030-nm . Instead of using a standard Gaussian beam as the input, we chose the amplitude/phase shaped beams for the demonstration. To precisely simulate the focusing conditions, we first record the intensity profile of the exotic beam at the entrance pupil of the objectives with an array of image sensors, and then calculate the amplitude distribution by take the square root of the intensity profile. Based on those measured 'user defined' amplitude profiles and their polarization states, we can achieve the complex fields on the entrance pupil by multiplying with the engineered phase information. Finally, based on Eq. (17) and Eq. (22), the fields near the focus can be calculated.

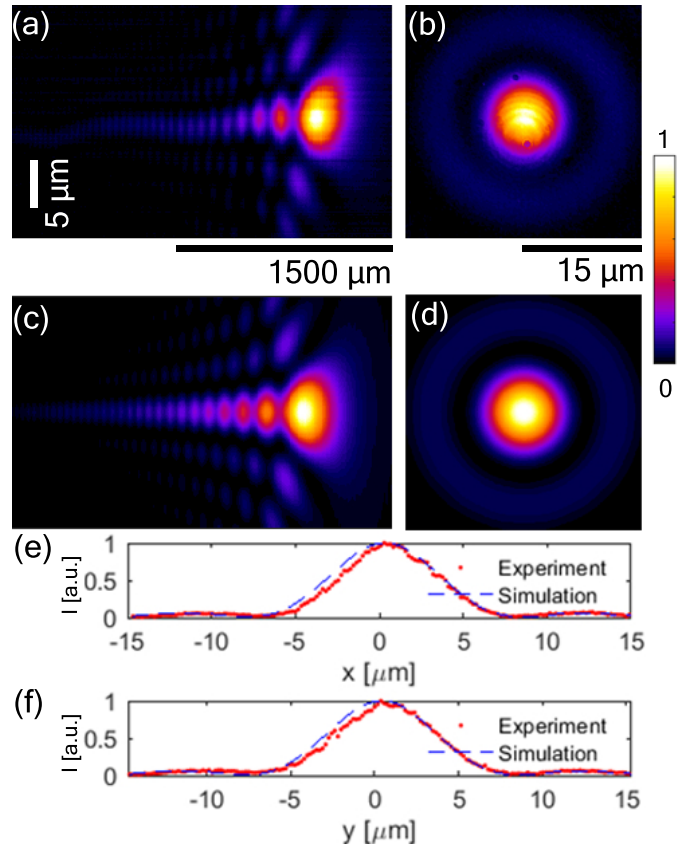


Fig. 4. Intensity distribution near the focus of a plano-convex lens (LA1951-C) in air with a Gaussian beam as the input. (a) Experimentally measured intensity along x-z plane; (b) experimentally measured intensity at the focal plane; (c) simulated intensity along x-z plane; (d) simulated intensity at the focal plane. And intensity profiles comparisons at the focal plane (e) along the x-axis; (f) along the y-axis.

These calculated intensity distributions are compared with the experimental results.

A circular cross-sectional focusing is often required for single-mode waveguides or microfluidic channels writing. Slit beam shaping is a simple technique that provides such isotropic resolution in transverse and vertical direction [39, 40]. In this section, we use the slit beam shaping as a first demonstration to prove that our methods are also applicable for the amplitude shaped beam.

As shown in Fig. 5 (a), a Gaussian beam with $1/e^2$ radius of 5.2 mm is cut by a 1.38-mm width slit. When this linear polarized beam is focused by the objective lens, the measured intensity distributions are shown in Fig. 5 (b-d) and the simulated results are shown in Fig. 5 (e-g). At the focal plane, as shown in Fig. 5 (d), the beam width along x-axis is measured as $2.9 \mu\text{m}$ and along y-axis is $10.9 \mu\text{m}$. Comparing with the simulated results shown in Fig. 5 (g), the beam widths exhibit the same value. By comparing the longitudinal results (b-c) and (e-f), the presented experimental and simulated focusing features are consistent, i.e. at first the laser beam is less tightly focused in y-z plane compare to the one in x-z plane and secondly the axis of the intensity center is tilt against z-axis. These features can be explained as at first the input beam is deficient filled the entrance pupil along y-axis and overfilled along x-axis which leads a relatively low effective

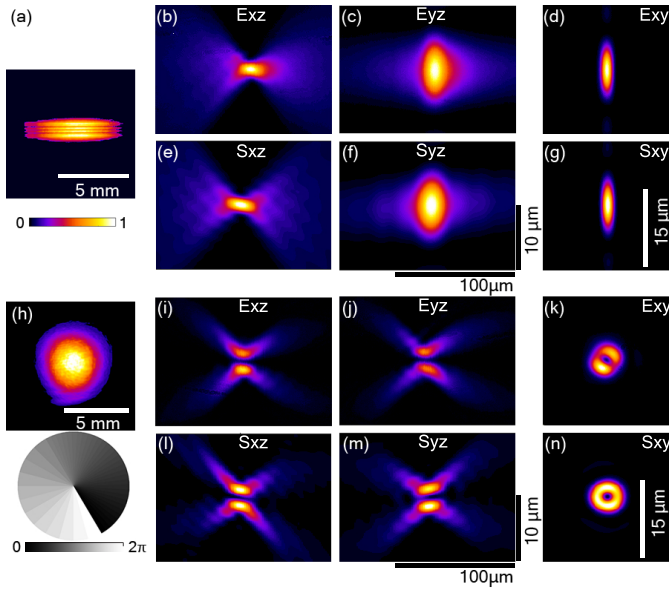


Fig. 5. Intensity and phase distribution of the input beam at the entrance pupil, (a) a Gaussian beam cut by a slit with a width of 1.38-mm, (h) a Gaussian beam pass through a spiral phase plate. Intensity distributions near the focus, (b-d) (i-k) experimentally measured intensity along x-z, y-z and x-y plane; (e-g) (l-n) simulated intensity along x-z, y-z and x-y plane.

NA in y direction, and secondly the input laser beam profile is rather than a perfect Gaussian distribution but exhibits some asymmetrical features. It is worth noting that the second feature is revealed in the simulation results only when it allows to use the real intensity distribution at the entrance pupil as the input. All in all, a nearly perfect match of the results empowered the model and the experimental method for investigating scenarios which have more sophisticated anisotropic input beams.

However, one should be careful when applying our computational method under the extremely asymmetric condition such as the line-focus microscopy (LTM), since Wolf has proposed that his Debye integral representation should be considered only beyond a critical value of the Fresnel number [41]. The Fresnel number is a dimensionless number, $\mathcal{N} = a^2/\lambda f$, which reflects the relative contribution of focusing vs. diffraction effects for a given aperture radius a , focal length f , and wavelength λ . For more rigorous approaches dedicated to this specific problem, one can refer to the works of De la Cruz *et al.* [42] and Lou *et al.* [43]. They have illustrated that when the Fresnel numbers close to unity the focus must shift backward, thus leading to astigmatic focusing when the circular symmetry of the input light is broken. In our case, the Fresnel number in y direction is as high as 41, which explains why we could not observe this backward shift in the experiment and makes our simulation results acceptable.

Moreover, phase shaping is also tested in this section. Over the last decade, the helical wavefront is one of the most extensively studied complex phase shapes of light. This type of light beams have an azimuthal phase dependence of $\exp(il\theta)$, where l is the topological charge. The optical vortex has many innovative applications in optical tweezers [44], atom manipulation [45] and material processing [46]. When focused, this optical vortex formed a ring instead of a spot on the focal plane. In this section,

experimentally, we used a spiral phase plate (SPP) to discretely generate an azimuthal phase distribution of $\exp(-il\theta)$. The topological charge is -1, and the number of discrete steps is 12. After the phase plate, the laser beam is focused by the same 20× objective lens. In the simulation, to obtain the corresponding complex field as the input, we multiplied the measured amplitude distribution with a discrete spiral phase map that exhibits the same phase distribution as the one used in experiment. The measured input intensity distribution and the calculated spiral phase map are presented in Fig. 5 (h).

The simulated results are shown in Fig. 5 (l-n). Comparing with the experimental results (i-k), it presents the same optical vortex feature. From the longitudinal intensity distributions (i-j) and (l-m) one can see that in both cases the light waves along the propagation axis cancel each other out and the ratios of the outer and inner radius are identical. At the focal plane, as shown in Fig. 5 (k) (n), this ratio is measured as 4.3 (experimental) and 4.0 (simulated). However, even in general the results achieved by the two methods are identical, one can still notice some deviations in terms of the spot ellipticity and the intensity homogeneity. Those deviations are most probably due to the imperfection of the spiral phase plate and its misalignment to the central of the beam.

D. Gaussian beam focused by objective lens in the bulk of silicon

In the previous sections, the laser beams are focused in the air. In this section, the in-bulk focus condition is chosen for demonstration. When a planar interface is present, according to aberration function Eq. (14), the interface-induced aberration is a function of the focus depth, the NA and the refractive index of the bulk material. When a Gaussian beam (λ : 1555-nm, $1/e^2$ radius: 5.2-mm) is focused into a 5-mm thick cubical crystalline silicon (c-Si) sample ($n = 3.475$ at 1555-nm) by an objective lens with NA of 0.65, the interface-induced aberration is prominent. Applying the same methods, we can achieve the experimental and simulated results of the longitudinal intensity distributions near the focus. When the focus depth is chosen as 5-mm and the propagation direction is from the left to the right, the experimental result is presented in Fig. 6 (a) and corresponding simulated result is shown in Fig. 6 (c). Differed from the previous cases, this comparison shows significant deviation, especially in terms of the overall length. The main reason of this deviation is that, as the propagation measurements procedures indicated, in a bulk material this measured result is actually not the intensity distribution with a focal depth of 5-mm. Precisely speaking, it is the stacking of intensity profiles at the exit surface of the 5-mm sample while the focusing objective lens moved step-by-step from -1.5 to +0.5 mm refers to the exit surface. To distinguish it from the real distribution in the bulk, Fig. 6 (b-c) show the simulated distribution with focal depth of 4-mm and 5-mm, comparing with the experimental result, the 4-mm result has a similar overall length but the relative intensity of the right-hand side 'tail' is much lower, and the 5-mm result shows a longer overall distribution length.

A spontaneous question raised here is 'why not directly measure the intensity distribution in the bulk?'. However, unfortunately, experimentally it is unlikely to measure the real intensity distribution. If we fix the position of the focusing objectives and move the recording microscope, the recorded images would also be affected by the depth related aberration during the step-by-step moving. The only way to avoid the artificial result is to compensate the depth related aberration after each movement.

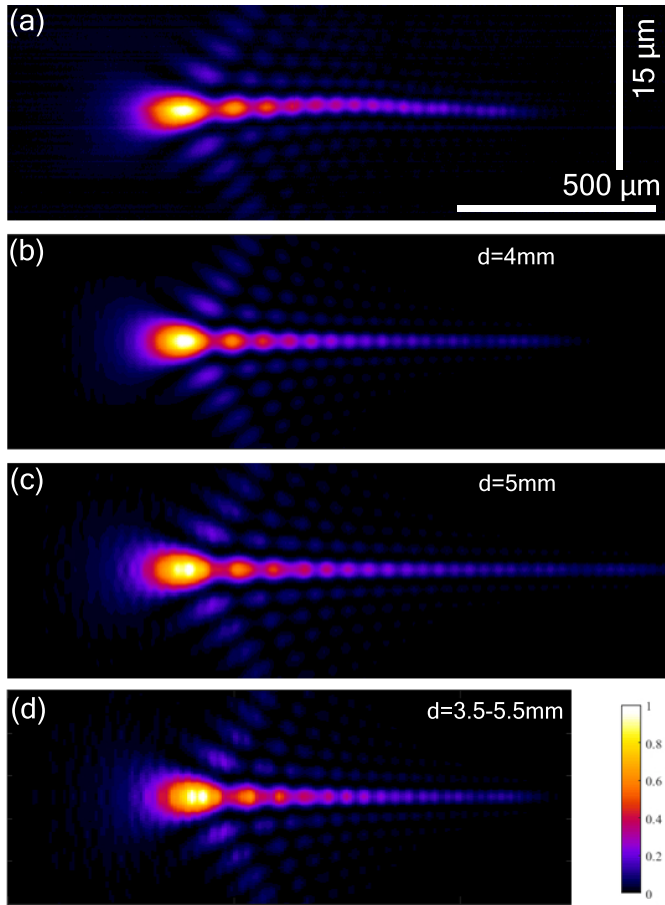


Fig. 6. Intensity distributions near the focus, (a) Experimentally measured intensity along x-z plane; (b-c) simulated intensity along x-z plane with focal depth of 4-mm and 5-mm; (d) simulated intensity at the exit surface of the 5-mm sample with focal depth varies from 3.5-mm to 5.5-mm.

Considering we have to move for more than two thousands steps during one measurement, it is unrealistic to compensate it with any simple tools such as correction collar. However, this measured result can still be helpful for benchmarking our simulation method.

In order to simulate the experimental condition, we first calculate the corresponding intensity profile at the exit surface of the 5-mm sample under different focal depths (from 3.5 to 5.5 mm). The focal depth increment step size is 5 μm . After the calculation, we stack the intensity profiles from the left to the right with the focal depth decrement from 5.5 mm to 3.5 mm. By taking those two steps, it simulates the image acquisition procedures of the experimental condition and the corresponding image intensity distribution is displaced in Fig. 6 (d). Compare to (b) and (c), it shows better similarity in terms of overall length and relative intensity along the profile to the experimental result (a).

Therefore, when a laser beam is focused into a bulk material, to investigate the intensity distribution along the propagation direction, one should pay extra attention for the results that obtained by the experimental methods.

To quantitatively illustrate the deviation of the experimental measured results and the actual in-bulk intensity distribution, and to get rid of the influence of the misalignment during the image frames acquisition, the simulated actual intensity distri-

bution profile is plot against simulated experimental result, i.e. Fig 6 (c) versus Fig 6 (d). The normalized profile comparison is presented in Fig 7 (b). The corresponding RMSD of this case is calculated as high as 0.113.

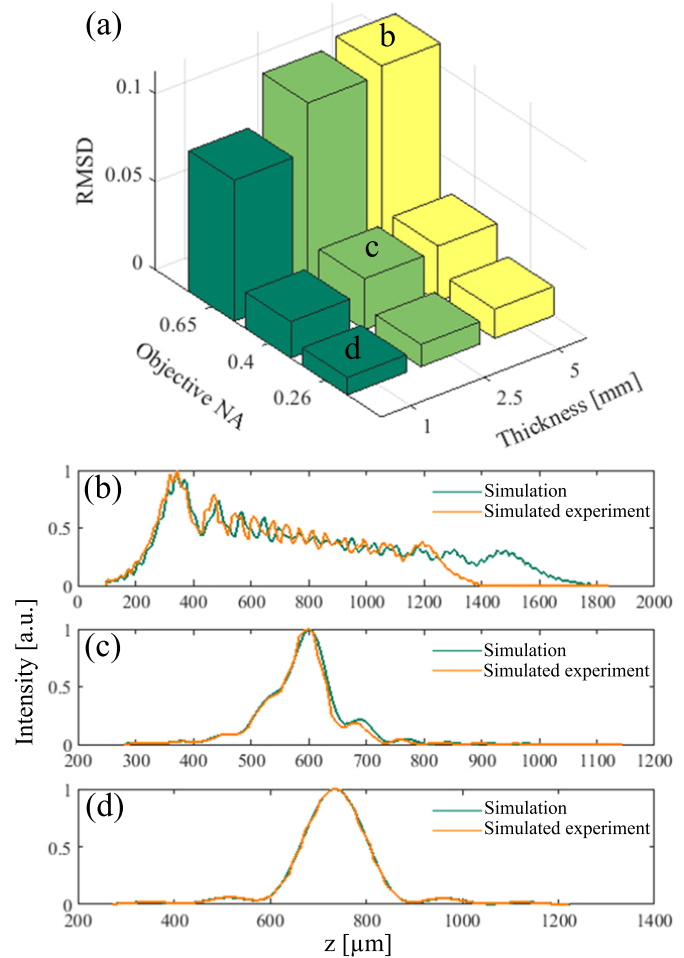


Fig. 7. (a) The RMSDs of the simulated actual intensity distribution and the simulated experimental result under different NAs and focal depths. Comparison of the cross-section intensity profiles near the focus along z-axis with (b) NA = 0.65 and focal depth of 5 mm; (c) NA = 0.4 and focal depth of 2.5 mm; (d) NA = 0.26 and focal depth of 1 mm.

Given that this deviation is caused by the aberration induced by the planar interface of the bulk material, the focus conditions (NA and focal depth) will determine how significant is this deviation. In order to illustrate this relationship and alert people the large deviation cases when applying similar propagation imaging methods, the RMSDs under different NAs and sample thicknesses are calculated and presented in Fig. 7 (a). As shown in the 3D bar chart, this deviation decreased when the NA of the objective lens or the focal depth decreased. In Fig. 7 (b-d) comparisons of the cross-section profiles along z-axis are illustrated under three selected cases. When the NA is decreased to 0.26 and the focal depth decreased to 1 mm, the experimental measured results are almost identical to the actual in-bulk intensity distribution. The RMSD for this case is 0.009. This value is even smaller than deviation of the experimental measured and simulated intensity distributions in the air, in which there is no

influence of the interface induced aberration. Therefore, in this case, it is safe to represent the actual intensity distribution by the experimental measured results and used this experimental tool to investigate more complicated nonlinear propagations problems [19].

5. CONCLUSION

In this paper, we introduced a benchmarked model and an experimental tool for analyzing the field distribution when a laser beam is focused in air or in any cubical materials. The vectorial analysis model considered the lens-induced as well as the planar interface-induced aberration. The in-bulk propagation imaging setup provides a 300-nm longitudinal resolution and diffraction limited lateral resolution. Using the tools introduced in this paper, people can deal with a variety of real focus conditions in which arbitrary input fields, non-aplanatic lens, and in-bulk focus might involve.

Besides, we have also pointed out that when the numerical aperture of the focusing element is high (e.g. > 0.4) and the focal depth is deep (e.g. > 2.5 mm), the experimental results acquired by the any propagation imaging methods that are similar to the one described in this paper might lead large deviation against the actual intensity distribution in the desired focal depth. One should calculate the RMSD or at least check the RMSD chart before applying these methods to any linear or nonlinear propagation imaging experiments.

APPENDIX A: ZERNIKE STANDARD COEFFICIENTS OF THE SINGLE LENS

This appendix listed the nonzero terms of the Zernike standard coefficients calculated at the exit pupil of the single lens LA1951-C and C240TME-C. For both lens, the properties of the incident laser beams are the same, i.e, a wavelength of 1555 nm and an $1/e^2$ radius of 5.2 mm. The refractive index of the medium after the lens is 1.

	LA1951-C	C240TME-C	Polynomials
Z_1	2.484	0.5821	1
Z_4	2.171	0.3187	$\sqrt{3}(2r^2 - 1)$
Z_{11}	0.581	-0.0209	$\sqrt{5}(6r^4 - 6r^2 + 1)$
Z_{22}	0.009	-0.007	$\sqrt{7}(20r^6 - 30r^4 + 12r^2 - 1)$
z_{37}	0.0002	-0.007	$\sqrt{9}(70r^8 - 140r^6 + 90r^4 - 20r^2 + 1)$

Table A1. Nonzero terms of the Zernike standard coefficients calculated at the exit pupil of a plano-convex lens Thorlabs LA1951-C and an aspherical lens C240TME-C.

REFERENCES

- Q. Li, "Infocus (version 1.0.0), <https://github.com/qf06/infocus>,".
- Y. Bellouard, A. Said, M. Dugan, and P. Bado, "Fabrication of high-aspect ratio, micro-fluidic channels and tunnels using femtosecond laser pulses and chemical etching," *Opt. express* **12**, 2120–2129 (2004).
- R. Osellame, V. Maselli, R. M. Vazquez, R. Ramponi, and G. Cerullo, "Integration of optical waveguides and microfluidic channels both fabricated by femtosecond laser irradiation," *Appl. physics letters* **90**, 231118 (2007).
- V. Maselli, J. R. Grenier, S. Ho, and P. R. Herman, "Femtosecond laser written optofluidic sensor: Bragg grating waveguide evanescent probing of microfluidic channel," *Opt. Express* **17**, 11719–11729 (2009).
- F. He, Y. Cheng, Z. Xu, Y. Liao, J. Xu, H. Sun, C. Wang, Z. Zhou, K. Sugioka, K. Midorikawa *et al.*, "Direct fabrication of homogeneous microfluidic channels embedded in fused silica using a femtosecond laser," *Opt. letters* **35**, 282–284 (2010).
- K. M. Davis, K. Miura, N. Sugimoto, and K. Hirao, "Writing waveguides in glass with a femtosecond laser," *Opt. letters* **21**, 1729–1731 (1996).
- M. Chambronneau, Q. Li, M. Chanal, N. Sanner, and D. Grojo, "Writing waveguides inside monolithic crystalline silicon with nanosecond laser pulses," *Opt. letters* **41**, 4875–4878 (2016).
- I. Pavlov, O. Tokel, S. Pavlova, V. Kadan, G. Makey, A. Turnali, Ö. Yavuz, and F. Ilday, "Femtosecond laser written waveguides deep inside silicon," *Opt. Lett.* **42**, 3028–3031 (2017).
- W. Gebremichael, L. Canioni, Y. Petit, and I. Manek-Hönniger, "Double-track waveguides inside calcium fluoride crystals," *Crystals* **10**, 109 (2020).
- X. Wang, X. Yu, M. Berg, B. DePaola, H. Shi, P. Chen, L. Xue, X. Chang, and S. Lei, "Nanosecond laser writing of straight and curved waveguides in silicon with shaped beams," *J. Laser Appl.* **32**, 022002 (2020).
- M. Chambronneau, D. Richter, S. Nolte, and D. Grojo, "Inscribing diffraction gratings in bulk silicon with nanosecond laser pulses," *Opt. Lett.* **43**, 6069–6072 (2018).
- J. Zhang, M. Gecevičius, M. Beresna, and P. G. Kazansky, "Seemingly unlimited lifetime data storage in nanostructured glass," *Phys. Rev. Lett.* **112**, 033901 (2014).
- A. Crespi, R. Ramponi, R. Osellame, L. Sansoni, I. Bongioanni, F. Sciarino, G. Vallone, and P. Mataloni, "Integrated photonic quantum gates for polarization qubits," *Nat. communications* **2**, 1–6 (2011).
- K. Lammers, M. Ehrhardt, T. Malendevych, X. Xu, C. Vetter, A. Alberucci, A. Szameit, and S. Nolte, "Embedded nanograting-based waveplates for polarization control in integrated photonic circuits," *Opt. Mater. Express* **9**, 2560–2572 (2019).
- S. Richter, F. Zimmermann, A. Tünnermann, and S. Nolte, "Laser welding of glasses at high repetition rates—fundamentals and prospects," *Opt. & Laser Technol.* **83**, 59–66 (2016).
- G. Zhang, J. Bai, W. Zhao, K. Zhou, and G. Cheng, "Interface modification based ultrashort laser microwelding between sic and fused silica," *Opt. express* **25**, 1702–1709 (2017).
- K. Cvecek, S. Dehmel, I. Miyamoto, and M. Schmidt, "A review on glass welding by ultra-short laser pulses," *Int. J. Extrem. Manuf.* **1**, 042001 (2019).
- E. Penilla, L. Devia-Cruz, A. Wieg, P. Martinez-Torres, N. Cuando-Espitia, P. Sellappan, Y. Kodera, G. Aguilar, and J. Garay, "Ultrafast laser welding of ceramics," *Science* **365**, 803–808 (2019).
- M. Chambronneau, Q. Li, V. Y. Fedorov, M. Blothe, K. Schaarschmidt, M. Lorenz, S. Tzortzakakis, and S. Nolte, "Taming ultrafast laser filaments for optimized semiconductor–metal welding," *Laser & Photonics Rev.* **n/a**, 2000433.
- R. Meyer, L. Froehly, R. Giust, J. Del Hoyo, L. Furfaro, C. Billet, and F. Courvoisier, "Extremely high-aspect-ratio ultrafast Bessel beam generation and stealth dicing of multi-millimeter thick glass," *Appl. Phys. Lett.* **114** (2019).
- A. Couairon and A. Mysyrowicz, "Femtosecond filamentation in transparent media," *Phys. Reports* **441**, 47–189 (2007).
- L. Bergé, S. Skupin, R. Nuter, J. Kasparian, and J.-P. Wolf, "Ultra-short filaments of light in weakly ionized, optically transparent media," *Reports on progress physics* **70**, 1633 (2007).
- E. G. Gamaly, L. Rapp, V. Roppo, S. Juodkazis, and A. V. Rode, "Generation of high energy density by fs-laser-induced confined microexplosion," *New J. Phys.* **15**, 025018 (2013).
- V. Y. Fedorov, M. Chanal, D. Grojo, and S. Tzortzakakis, "Accessing extreme spatiotemporal localization of high-power laser radiation through

- transformation optics and scalar wave equations," *Phys. review letters* **117**, 043902 (2016).
25. P. K. Sahoo, T. Feng, and J. Qiao, "Dynamic pulse propagation modelling for predictive femtosecond-laser-microbonding of transparent materials," *Opt. Express* **28**, 31103–31118 (2020).
 26. J. Liu, B. Xu, and T. C. Chong, "Three-dimensional finite-difference time-domain analysis of optical disk storage system," *Jpn. J. Appl. Phys.* **39**, 687 (2000).
 27. A. Couairon, O. G. Kosareva, N. Panov, D. Shipilo, V. Andreeva, V. Jukna, and F. Nesa, "Propagation equation for tight-focusing by a parabolic mirror," *Opt. express* **23**, 31240–31252 (2015).
 28. D. E. Shipilo, I. A. Nikolaeva, V. Y. Fedorov, S. Tzortzakis, A. Couairon, N. A. Panov, and O. G. Kosareva, "Tight focusing of electromagnetic fields by large-aperture mirrors," *Phys. Rev. E* **100**, 033316 (2019).
 29. P. Varga and P. Török, "Focusing of electromagnetic waves by paraboloid mirrors. i. theory," *JOSA A* **17**, 2081–2089 (2000).
 30. P. Varga and P. Török, "Focusing of electromagnetic waves by paraboloid mirrors. ii. numerical results," *JOSA A* **17**, 2090–2095 (2000).
 31. M. Leutenegger, R. Rao, R. A. Leitgeb, and T. Lasser, "Fast focus field calculations," *Opt. express* **14**, 11277–11291 (2006).
 32. J. Lin, O. G. Rodríguez-Herrera, F. Kenny, D. Lara, and J. C. Dainty, "Fast vectorial calculation of the volumetric focused field distribution by using a three-dimensional Fourier transform," *Opt. Express* **20**, 1060 (2012).
 33. B. Richards and E. Wolf, "Electromagnetic diffraction in optical systems, ii. structure of the image field in an aplanatic system," *Proc. Royal Soc. London. Ser. A. Math. Phys. Sci.* **253**, 358–379 (1959).
 34. P. Török, P. Varga, Z. Laczik, and G. Booker, "Electromagnetic diffraction of light focused through a planar interface between materials of mismatched refractive indices: an integral representation," *JOSA A* **12**, 325–332 (1995).
 35. J. L. Bakx, "Efficient computation of optical disk readout by use of the chirp z transform," *Appl. Opt.* **41**, 4897 (2002).
 36. R. J. Noll, "Zernike polynomials and atmospheric turbulence," *J. Opt. Soc. Am.* **66**, 207 (1976).
 37. Q. Li, M. Chambonneau, M. Chanal, and D. Grojo, "Quantitative-phase microscopy of nanosecond laser-induced micro-modifications inside silicon," *Appl. optics* **55**, 9577–9583 (2016).
 38. A. Wang, A. Das, D. Grojo *et al.*, "Ultrafast laser writing deep inside silicon with thz-repetition-rate trains of pulses," *Research* **2020**, 8149764 (2020).
 39. Y. Cheng, K. Sugioka, K. Midorikawa, M. Masuda, K. Toyoda, M. Kawachi, and K. Shihoyama, "Control of the cross-sectional shape of a hollow microchannel embedded in photostructurable glass by use of a femtosecond laser," *Opt. letters* **28**, 55–57 (2003).
 40. M. Ams, G. Marshall, D. Spence, and M. Withford, "Slit beam shaping method for femtosecond laser direct-write fabrication of symmetric waveguides in bulk glasses," *Opt. express* **13**, 5676–5681 (2005).
 41. E. Wolf and Y. Li, "Conditions for the validity of the debye integral representation of focused fields," *Opt. Commun.* **39**, 205–210 (1981).
 42. A. R. De la Cruz, A. Ferrer, J. Del Hoyo, J. Siegel, and J. Solis, "Modeling of astigmatic-elliptical beam shaping during fs-laser waveguide writing including beam truncation and diffraction effects," *Appl. Phys. A* **104**, 687–693 (2011).
 43. K. Lou, S. Granick, and F. Amblard, "How to better focus waves by considering symmetry and information loss," *Proc. Natl. Acad. Sci.* **115**, 6554–6559 (2018).
 44. M. Padgett and R. Bowman, "Tweezers with a twist," *Nat. photonics* **5**, 343–348 (2011).
 45. K. Ladavac and D. G. Grier, "Microoptomechanical pumps assembled and driven by holographic optical vortex arrays," *Opt. Express* **12**, 1144–1149 (2004).
 46. C. Hnatovsky, V. G. Shvedov, W. Krolkowski, and A. V. Rode, "Materials processing with a tightly focused femtosecond laser vortex pulse," *Opt. letters* **35**, 3417–3419 (2010).